Assessment of SCaMPR and NEXRAD Q2 Precipitation Estimates Using Oklahoma Mesonet Observations

RONALD STENZ, XIQUAN DONG, AND BAIKE XI

Department of Atmospheric Sciences, University of North Dakota, Grand Forks, North Dakota

ROBERT J. KULIGOWSKI

NOAA/NESDIS/Center for Satellite Applications and Research, College Park, Maryland

(Manuscript received 4 December 2013, in final form 17 January 2014)

ABSTRACT

Although satellite precipitation estimates provide valuable information for weather and flood forecasts, infrared (IR) brightness temperature (BT)-based algorithms often produce large errors for precipitation detection and estimation during deep convective systems (DCSs). As DCSs produce greatly varying precipitation rates below similar IR BT retrievals, using IR BTs alone to estimate precipitation in DCSs is problematic. Classifying a DCS into convective-core (CC), stratiform (SR), and anvil cloud (AC) regions allows an evaluation of estimated precipitation distributions among DCS components to supplement typical quantitative precipitation estimate (QPE) evaluations and to diagnose these IR-based algorithm biases. This paper assesses the performance of the National Mosaic and Multi-Sensor Next Generation Quantitative Precipitation Estimation System (NMQ Q2), and a simplified version of the Self-Calibrating Multivariate Precipitation Retrieval (SCaMPR) algorithm, over the state of Oklahoma using Oklahoma Mesonet observations. While average annual Q2 precipitation estimates were about 35% higher than Mesonet observations, strong correlations exist between these two datasets for multiple temporal and spatial scales. Additionally, the Q2-estimated precipitation distribution among DCS components strongly resembled the Mesonet-observed distribution, indicating Q2 can accurately capture the precipitation characteristics of DCSs despite its wet bias. SCaMPR retrievals were typically 3–4 times higher than Mesonet observations, with relatively weak correlations during 2012. Overestimates from SCaMPR retrievals were primarily caused by precipitation retrievals from the anvil regions of DCSs when collocated Mesonet stations recorded no precipitation. A modified SCaMPR retrieval algorithm, employing both cloud optical depth and IR temperature, has the potential to make significant improvements to reduce the wet bias of SCaMPR retrievals over anvil regions of a DCS.

1. Introduction

In addition to rain gauge networks, sources for quantitative precipitation estimates (QPEs) such as satellites and ground-based radars are critical to the National Oceanic and Atmospheric Administration (NOAA)/National Weather Service (NWS) flood and river forecasts (Zhang and Qi 2010; Zhang et al. 2011). Rain gauge networks face limitations in spatial coverage, and radar estimates have problems with beam blockage and overshooting along with limited spatial coverage (Krajewski and Smith 2002; Scofield and Kuligowski 2003; Smith et al. 1996; Zhang and Qi 2010; Zhang et al. 2011). QPEs derived from geostationary satellites such as the Self-Calibrating Multivariate Precipitation Retrievals (SCaMPR) can help address spatial gaps by providing continuous spatial coverage (Scofield and Kuligowski 2003). This advantage of satellite QPEs has led to their incorporation into the multisensor precipitation estimation algorithm (Kondragunta et al. 2005). Potential applications of near-real-time satellite QPEs for disaster preparedness and mitigation are possible at both regional and global scales (Hong et al. 2007).

Corresponding author address: Professor Xiquan Dong, Department of Atmospheric Sciences, University of North Dakota, 4149 University Ave., MS 9006, Grand Forks, ND 58203-9006.
E-mail: dong@aero.und.edu

DOI: 10.1175/JHM-D-13-0199.1

© 2014 American Meteorological Society

The relationship between the satellite-retrieved, IR brightness temperatures of storms and precipitation rates at the surface has been well documented especially for convection, and methods utilizing IR brightness temperatures to estimate precipitation have been developed and modified over the last three decades (e.g., Negri and Adler 1981; Adler and Negri 1988; Vicente et al. 1998). The current operational satellite rainfall estimation algorithm at the NOAA National Environmental Satellite, Data, and Information Service (NESDIS) is the Hydro-Estimator (H-E), which estimates precipitation from geostationary platforms by relating IR brightness temperatures to precipitation rates (Scofield and Kuligowski 2003). The next-generation operational NOAA/NESDIS algorithm for the Geostationary Operational Environment Satellite R series (GOES-R), SCaMPR, employs IR brightness temperature and microwave data to retrieve rainfall rates (Kuligowski 2010). Numerous other real-time algorithms exist for retrieving rainfall rates from IR and microwave data, including the Climate Prediction Center morphing technique (CMORPH) (Joyce et al. 2004); Global Satellite Mapping of Precipitation, version Moving Vector with Kalman (GSMaP_MVK+; the plus sign refers to the version that utilizes rainfall estimates from the AMSU-B sensor in addition to PMW images) (Kubota et al. 2007); the Naval Research Laboratory (NRL) blended algorithm (Turk et al. 2003); Precipitation Estimation from Remotely Sensed Imagery Using Artificial Neural Networks (PERSIANN) (Sorooshian et al. 2000); and the Tropical Rainfall Measuring Mission (TRMM) Multisatellite Precipitation Analysis (TMPA) (Huffman et al. 2007). However, this paper will focus on evaluating SCaMPR in preparation for its operational application at NOAA/NESDIS.

As a large portion of rainfall and the majority of severe weather reports in the United States arise from deep convective systems (DCSs), improved understanding and satellite QPEs of these systems are important. DCSs can be separated into convective-core (CC), stratiform (SR), and anvil cloud (AC) regions, with the most intense precipitation in CC regions, light to moderate precipitation in the SR regions, and light or no precipitation in AC regions, using a hybrid classification algorithm (Feng et al. 2011, 2012; section 2d). This hybrid classification product is produced over a grid resolution of 4 km × 4 km and is available with the same temporal resolution as SCaMPR instantaneous estimates.

To improve satellite-derived QPEs during DCSs, a source of validation data is needed with significantly better spatial and temporal coverage and resolution than what rain gauge networks provide. Recent studies such as Kirstetter et al. (2012) and Amitai et al. (2012) have utilized ground-based radar estimates as a validation source for TRMM. Even more detailed validation and analysis can be achieved using a combination of Next Generation Weather Radar (NEXRAD) observations and GOES satellite retrievals to classify the three components of a DCS (Feng et al. 2011, 2012), which provides some guidance to improve the spatial precipitation characteristics of satellite QPEs such as SCaMPR. Since the size of the anvil area of a DCS is highly variable, and the IR brightness temperatures over anvil regions are similar to those over convective cores (Feng et al. 2011, 2012), effectively separating the anvil from rain-core regions prior to calculating IR-based precipitation rates could significantly improve geostationary satellite QPEs (Vicente et al. 1998). Using a combination of the National Mosaic and Multi-Sensor Next Generation Quantitative Precipitation Estimation System (NMQ Q2) and GOES data, DCSs can be broken into three components that allow a better evaluation of the strengths and weaknesses of SCaMPR retrievals. With the hybrid classification, the distribution of precipitation among the DCS components can be calculated for SCaMPR retrievals and compared to observed values from Mesonet observations. This analysis will provide statistics for the precipitation distribution in DCSs and will also quantify the SCaMPR wet bias in non-rain-core regions for the first time. Findings from these evaluations could eventually improve separation of anvil and rain-core regions using only geostationary satellite retrievals. Furthermore, this method of analysis using the hybrid classification system can be used to quantitatively evaluate potential improvements in future algorithms addressing the wet bias of IR-based precipitation retrievals in non-rain-core regions. However, the uncertainties and errors in radar-derived Q2 estimates and satellite-derived precipitation products must first be properly analyzed and validated with ground-based rain gauge measurements that can provide independent "ground truth."

Many uncertainties involved in radar precipitation estimates and attempts to mitigate these uncertainties have been discussed in previous studies (Andrieu et al. 1997; Austin 1987; Langston et al. 2007; Villarini and Krajewski 2010; Smith et al. 1996; Zhang et al. 2005; Zhang and Qi 2010; Zhang et al. 2011). In a recent evaluation of the NMQ and the Precipitation Processing System (PPS) over the conterminous United States (CONUS), Wu et al. (2012) found that NMQ estimates performed better on average than the PPS over the CONUS and during heavy precipitation events. While the findings of Wu et al. (2012) and Chen et al. (2013) support the use of NMQ Q2 estimates as the primary dataset for improving satellite QPEs, an evaluation of the magnitude of NMQ Q2 errors and their biases over longer

time periods is necessary against a dense rain gauge network in a region where precipitation is largely from DCSs. Furthermore, although the distribution of precipitation into different reflectivity–rain rate (Z–R) regimes has been studied (Chen et al. 2013), analysis of the distribution of estimated precipitation in DCS regions is needed to quantitatively examine the errors and biases of satellite QPEs.

Recently, the NWS has upgraded its radar network to include dual-polarization technology. Dual-polarization radar transmits energy in both the horizontal and vertical directions and provides more information about targeted hydrometeors than a single-polarization radar provides. Thorough overviews of dual polarization are already available in literature (Islam and Rico-Ramirez 2013), so only a brief summary of dual-polarization applications to the hybrid classification (Feng et al. 2011) and Q2 estimates will be discussed in this study. While the Q2 algorithm utilizes only horizontal polarization, some incorporation of dual-polarization technology could aid in removing ground clutter contamination in radar precipitation estimates (Zrnić et al. 2006). This could be useful for filtering out erroneous light precipitation estimates that occur from inversion-induced ground clutter. In Q3, an updated version of Q2, dual-polarization technology has been incorporated for more accurate hydrometeor identification (Zhang et al. 2014). Additionally, hail-core classifications could be added to the current hybrid classification algorithm developed by Feng et al. (2011) by utilizing the hydrometeor classifications developed for the Weather Surveillance Radar-1988 Doppler (WSR-88D) (Park et al. 2009). As hail cores are a significant part of DCSs, this revised classification algorithm would allow a more detailed examination of DCS structures and their life cycles.

To evaluate both NMQ Q2 estimates and SCaMPR retrievals in a region with precipitation dominated by DCSs, Oklahoma (OK) Mesonet-observed precipitation has been used as ground truth in this study. This study will use time scales from 24-h to annual precipitation to examine the performance of SCaMPR retrievals and Q2 estimates for both individual precipitation events and longer time scales. The NMQ Q2 estimates during the period 2010–12 will be directly compared to collocated Oklahoma Mesonet observations to determine the accuracy, consistency, and any biases associated with Q2 estimates. The same analysis will be performed on SCaMPR for 2012 data to evaluate the performance of SCaMPR retrievals and possible sources of error. Potential causes for any biases or errors will be examined along with possible methods of improvement. Special attention will be given to the absolute accuracy of Q2 estimates and scenarios where SCaMPR retrievals produced significant overestimates. Additionally, precipitation distributions will be calculated for each of the DCS regions from both observations and estimates. This will provide a quantitative insight into the precipitation characteristics of DCSs, while also evaluating the accuracy of both Q2 and SCaMPR precipitation estimates in providing reasonable precipitation distributions for DCSs. By examining the estimated precipitation distribution from SCaMPR, the cause of errors can be diagnosed and more precisely accounted for and corrected than when using only qualitative studies. Furthermore, an evaluation of the estimated precipitation distribution from Q2 can determine how reasonable a substitute for ground truth this product is where dense rain gauge networks are unavailable.

By evaluating the performance of both SCaMPR and Q2, this study will explore potential pathways for improvements of satellite QPEs during DCSs in a more targeted approach than previous studies. The accuracy of Q2 in a region with annual precipitation dominated by convection will first be examined to determine how reliable of a substitute Q2 estimates can be for calibrating satellite QPEs when a higher-resolution validation dataset is needed compared to what rain gauge networks provide. Next, SCaMPR estimates will be evaluated on multiple temporal and spatial scales to pinpoint the sources of bias and error for this IR-based satellite QPE. Last, a discussion of the findings from this study and preliminary results from a newly developed method to correct the biases/errors of SCaMPR will be provided.

2. Data and methodology

a. *NEXRAD Q2 data*

The NMQ Q2 tile 6 estimates from January 2010 to December 2012 were compared with Oklahoma Mesonet observations and SCaMPR retrievals. NMQ tile 6 has northern and southern boundaries at 40° and 20°N and is bounded longitudinally by 110° and 90°W. NMQ Q2 estimates provide multiradar precipitation estimates with a grid resolution of 1 km × 1 km (www.nssl.noaa.gov/projects/q2/q2.php). Q2 estimates are produced using quality-controlled radar reflectivity data from multiple radars to automatically classify precipitation as convective rain, stratiform rain, warm rain, hail, and snow (Zhang et al. 2011). These classifications will assign *Z–R* relationships to each pixel to provide the Q2-estimated rain rates (Zhang et al. 2011). These pixel-level estimates can be easily compared to collocated Oklahoma Mesonet observations. The large spatial coverage and high spatial resolution of the NEXRAD Q2 estimates will provide some guidance to assess (and

potentially improve) the performance of the SCaMPR retrievals over large areas with a much finer resolution than rain gauge networks.

b. Oklahoma Mesonet

Oklahoma Mesonet 24-h accumulated precipitation from January 2010 to December 2012 was used as the ground truth in this study. There are a total of 119 Mesonet stations with data spanning the entire time period for this study. Potential time mismatch problems during frozen precipitation events were minimal because frozen precipitation typically accounts for ~1% of annual precipitation in the study region during this study (www.ncdc.noaa.gov/).

c. SCaMPR retrievals

The GOES-R algorithm for rain detection and estimation, SCaMPR, attempts to capture the accuracy of microwave (MW) rain rates along with the rapid refresh of GOES data by calibrating GOES IR-based predictors against MW rainfall (Kuligowski 2010). Separately matched datasets for four latitude bands and three cloud types (determined using brightness temperature differences between bands) are updated every time new MW rain rates become available and the oldest data are removed. Whenever the matched datasets are updated, discriminant analysis is used to identify the two best predictors and coefficients for discriminating raining from nonraining pixels; stepwise forward linear regression is used to select the two best predictors and coefficients for deriving rain rates. To account for the nonlinear relationship between IR brightness temperatures and rain rates, the former are regressed against the latter in log–log space to produce additional rain-rate predictors. To compensate for the compression of the statistical distribution that results from applying regression techniques to nonnormally distributed data, the cumulative distribution functions (CDFs) of the rain rates derived via regression from dependent data are matched against the CDFs of the MW rain rates to create a lookup table that restores the retrieved rain rates to the correct distribution. Please refer to Kuligowski (2010) for additional details.

The full version of SCaMPR was developed using five bands from the Meteosat Spinning Enhanced Visible Infrared Imager (SEVIRI)—the water vapor bands at 6.2 and 7.3 μm and the IR window bands at 8.7, 10.8, and 12.0 μm. However, the version of SCaMPR evaluated in this paper was simplified from the full version because only two of the five bands used by the algorithm are available on the current GOES—one water vapor band at 6.7 μm and one IR window band at 10.7 μm; among other changes, this meant that only two cloud types existed instead of three, and the available predictor dataset was reduced by half. SCaMPR precipitation retrievals were only available from January to December 2012 with a grid resolution of 4 km × 4 km and complete coverage of Oklahoma.

d. Hybrid classification method

Feng et al. (2011) developed a method to objectively identify DCSs and subsequently classify their convective core, stratiform regions, and anvil regions through an integrative analysis of collocated, ground-based, scanning radar and geostationary satellite data over the southern Great Plains (SGP) region. Detailed and accurate classification of these DCS components provided by this method can be used to better quantitatively evaluate the estimated/retrieved precipitation distributions among DCS components to supplement typical QPE evaluations and to diagnose IR-based algorithm biases. The CC region can be identified by radar and is characterized by high reflectivity values using the convective–stratiform algorithm originally developed in Steiner et al. (1995) and modified by Feng et al. (2011). For this study, the threshold for a pixel to be identified as a CC was set to 45 dBZ. The SR region identified by radar accounts for precipitation echoes that fall below the convective dBZ threshold (Steiner et al. 1995). AC regions can partially be identified by radar, typically by using an echo-height threshold, 6 km in this study, but limited power returns from anvil regions frequently make these clouds undetectable by ground-based precipitation radars such as the WSR-88D. However, GOES satellites can detect the entire cloud shield, including regions of the anvil, typically thin anvil, which is undetectable by radar. GOES data were used to supplement the WSR-88D data when identifying anvil regions of DCSs in this study. This hybrid classification product is produced over a grid resolution of 4 km × 4 km and is available with the same temporal resolution as SCaMPR instantaneous estimates. An example output from the radar-only classification (Fig. 1a) and combined radar and satellite (Fig. 1b) illustrates the contribution geostationary satellite data make in the hybrid classification.

e. Methodology of evaluation

When evaluating NMQ Q2 estimates and SCaMPR retrievals, Oklahoma Mesonet observations were treated as ground truth. After determining that pixels on the NMQ and SCaMPR grids corresponded with the Mesonet locations, the NMQ Q2 estimates and SCaMPR retrievals were directly compared to collocated Mesonet observations. Comparisons were only made when both datasets were available, such as Q2 versus Mesonet during 2010–12 and SCaMPR versus Mesonet in 2012.

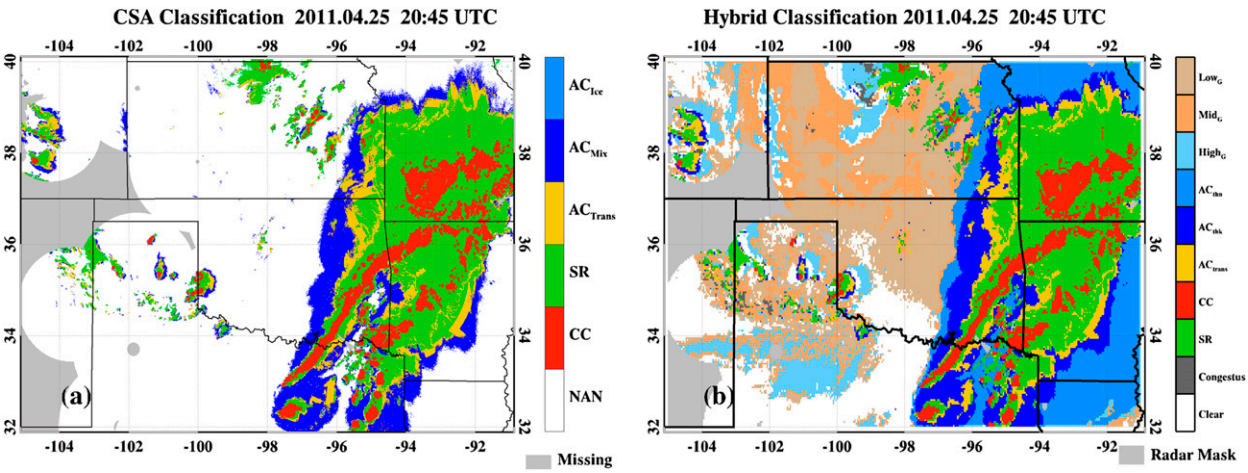

FIG. 1. Examples of the classification output (a) from radar only and (b) using the hybrid combination of radar and satellite.

Scatterplots were constructed between the Q2 estimates and Mesonet observations when Mesonet observations had recorded precipitation (≥0.25 mm, the minimum detectable value for the Mesonet rain gauges). Regression lines were derived for two spatial scales: 1) the 24-h accumulated and annual precipitation from each Mesonet station and 2) the statewide 24-h total precipitation from all Mesonet stations. Since radar coverage variation has been well documented over the United States (Maddox et al. 2002), this study was also performed only for those Mesonet stations in regions of good radar coverage; that is, the bottom of the radar base beam was ≤1219 m AGL (generally within ~130 km of the radar location).

Additionally, comparisons between the Q2 estimates and Mesonet observations were made for both the warm and cold seasons. The warm season was defined as April–September, while the cold season was from October to March (Wu et al. 2012). These seasons help broadly separate precipitation characteristics to evaluate the accuracy of Q2 estimates for precipitation dominated by convection during the warm season and the typical widespread and stratiform precipitation during the cold season (http://cig.Mesonet.org/climateatlas/doc60.html). Scatterplots were created for 24-h precipitation estimates and observations during both the warm and cold seasons along with their corresponding linear regression equations. The same comparison between the SCaMPR retrievals and Mesonet observations was done only for 2012.

In addition to regressing the Q2-estimated and SCaMPR-retrieved precipitation against Mesonet observations, cumulative frequency distributions were constructed for each of the datasets. To construct the cumulative distribution functions, a total of 50 2-mm bins were generated from all available samples for each dataset. To visually compare the CFDs of the precipitation amount, the percentages of precipitation events in each Mesonet bin were subtracted from the percentages of precipitation events in the corresponding Q2 estimate or SCaMPR retrieval bins. Finally, categorical scores were calculated for both NMQ Q2 estimates and SCaMPR retrievals using four thresholds of Mesonet rainfall accumulation for the false alarm rate (FAR), probability of detection (POD), and critical success index (CSI). The categorical scores are calculated as follows. POD is defined as the ratio of hits to the sum of misses and hits. Each hit represents an occurrence of an estimate greater than the threshold value when Mesonet-observed precipitation also exceeds the threshold value. A miss represents an occurrence of an estimate less than the threshold value when Mesonet-observed precipitation exceeds the threshold value. FAR is defined as false alarms divided by the sum of false alarms and hits. A false alarm represents an occurrence of an estimate greater than the threshold value when Mesonet-observed precipitation did not exceed the threshold value. Last, CSI is defined as the ratio of hits to the sum of hits, misses, and false alarms. The threshold values were 0.25, 2.5, 12.5, and 25 mm for 24-h accumulated precipitation events spanning 3 years of NMQ Q2 estimates and 1 year of SCaMPR retrievals. Root-mean-square error (RMSE) values were calculated for 24-h precipitation events with four threshold values. Additionally, RMSE scores were calculated for the annual average and for 2012 when both SCaMPR and Q2 data were available.

To analyze the precipitation characteristics of DCSs and to evaluate Q2 and SCaMPR performance in DCSs, precipitation distributions were calculated from

Mesonet observations and from SCaMPR and Q2 estimates. DCS components (CC, SR, and AC) were classified using NEXRAD and GOES data (Feng et al. 2011, 2012) over OK. All SCaMPR and Q2 pixels were matched with the classified components, and their corresponding precipitation distributions were then calculated based on the sum of rates for each classified pixel. For the Mesonet precipitation distribution, the classification over each Mesonet station was matched with the 5-min accumulated precipitation ending at the time of the classification. There was little sensitivity between choosing the 5-min accumulation starting/ending at the time of the DCS classification.

3. Results

a. Q2 versus Mesonet

Figure 2 shows the scatterplots of 24-h accumulated precipitation from collocated Oklahoma Mesonet observations and Q2 estimates during the period 2010–12. There are a total of 27 201 samples when precipitation was recorded by a Mesonet station (≥0.25 mm) and Q2 estimates were also available. A linear relationship between the two datasets was found, providing a strong correlation of 0.881. On average, Q2 estimates were about 25.6% higher than Mesonet observations (Fig. 2a), mainly because of contributions by the warm season (April–September) when Q2 estimates had a positive bias of 37.9% (Fig. 2b). During the cold season (October–March), however, an excellent agreement (~5%) was reached between the two datasets (Fig. 2c). The sample sizes during the warm and cold seasons were nearly equal, and their correlations were also similar. There were more intense precipitation events during the warm season than during the cold season; as a result, the mean 24-h accumulated precipitation from Mesonet observations increased from 7.42 to 10.66 mm (43.7%) from the cold to warm season, while Q2 estimates increased from 7.81 to 14.70 mm (88.2%). The excellent agreement during the cold season indicates that the Q2 precipitation estimates from NEXRAD reflectivity are reasonable for stratiform-dominated precipitation. The Q2-estimated precipitation during the warm season, however, produced overestimates. These overestimates are likely attributed to incorrect classifications of tropical rain in the Q2 algorithm (Chen et al. 2013) and possibly from increased reflectivity due to hail and graupel (Wu et al. 2013).

Figure 3 compares the CFDs of 24-h accumulated precipitation and the percentage differences (Q2 − Mesonet) for each bin from a total of 125 543 collocated Q2 estimates and Mesonet observations during the 3-yr

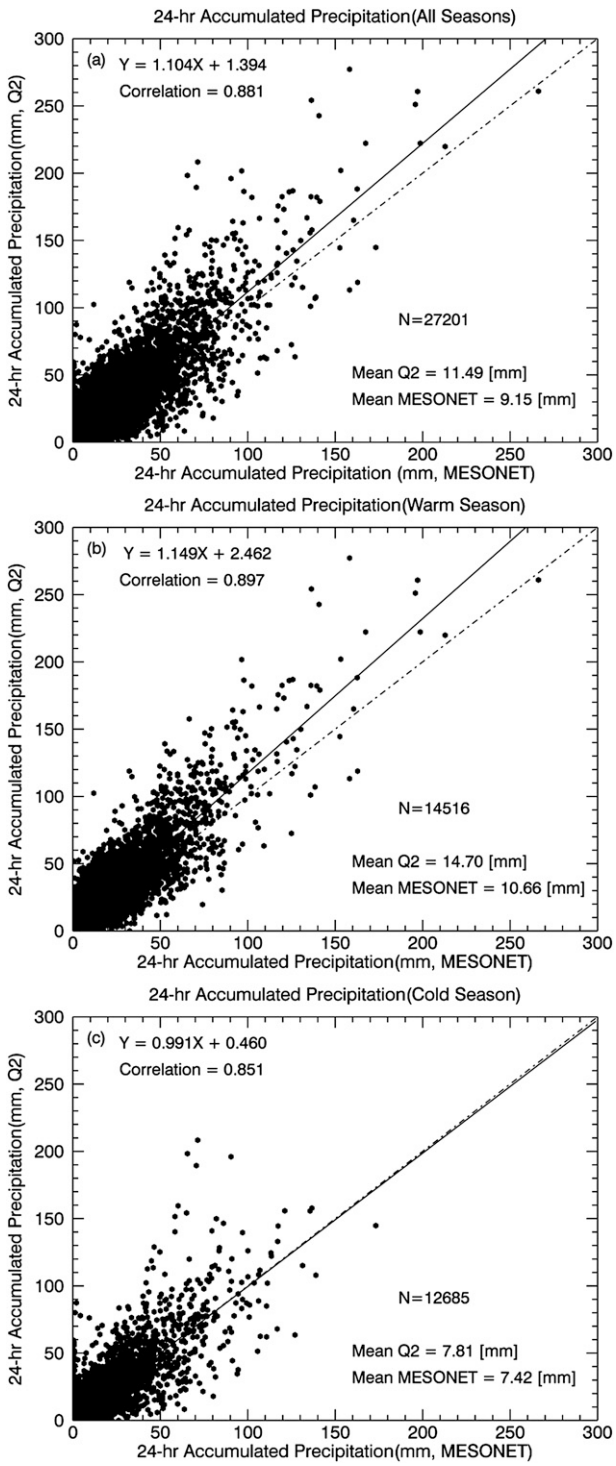

FIG. 2. Each dot represents a pair of collocated Mesonet-observed and Q2-estimated 24-h accumulated precipitation (rainfall >0.25 mm; i.e., excluding nonprecipitating events at each Mesonet station) during the period 2010–12. Shown are (a) all available collocated Mesonet and Q2 observations, (b) the warm season (April–September), and (c) the cold season (October–March).

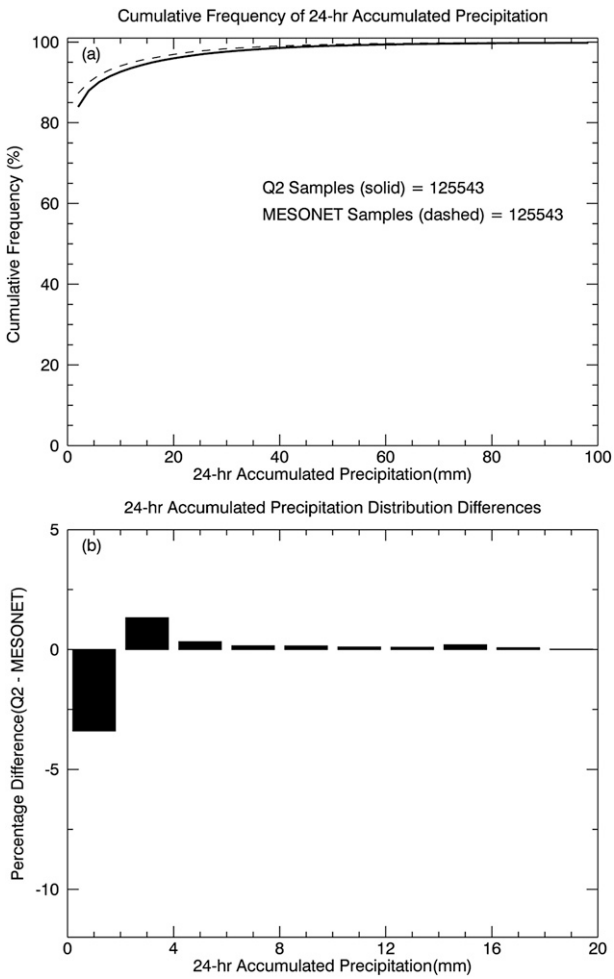

FIG. 3. (a) Cumulative frequency of 24-h accumulated precipitation from all samples (rainfall ≥0 mm) during the period 2010–12. Both Mesonet and Q2 samples were sorted into 50 2-mm bins. (b) The percentages of the samples of each bin to total samples (3 yr × 365 days × 119 stations) for both Mesonet and Q2 are calculated, respectively, and their percentage differences (Q2 − Mesonet) for each bin are calculated until bin 10 (up to 20 mm; after that the percentage differences are negligible).

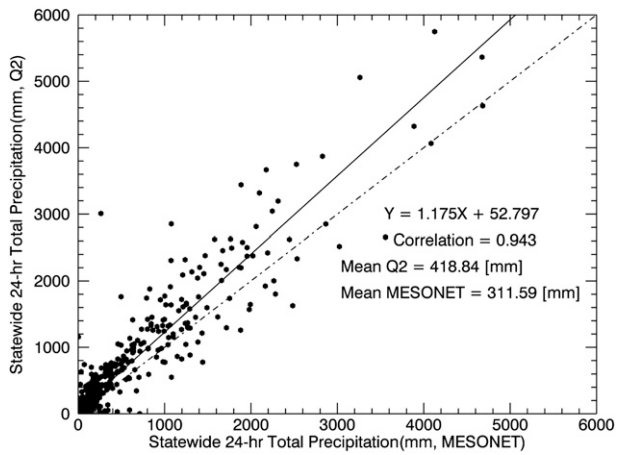

FIG. 4. Each dot represents 24-h total precipitation (statewide rainfall ≥0.25 mm; i.e., excluding nonprecipitating events) from all Oklahoma Mesonet stations and collocated Q2 estimates during the period 2010–12 (N = 798).

period. As opposed to the samples in Fig. 2 (rainfall ≥ 0.25 mm), the total samples in Fig. 3 include all collocated Q2 estimates and Mesonet observations; that is, nonprecipitating events are included in Fig. 3. These samples were sorted into 50 2-mm bins where both Mesonet and Q2 CFDs were dominated by their first bin (0–2 mm, ~85%) because the nonprecipitating events were included in this bin. Both CFDs approached 100% with very similar slopes as the precipitation amounts of the bins increased (Fig. 3a). The corresponding percentages of the samples in each bin to total samples (~3 yr × 365 days × 119 stations) for both Mesonet and Q2 were calculated first, and then their percentage differences (Q2 − Mesonet) for each bin were calculated and shown in Fig. 3b. The largest difference occurred in the first bin, 0–2 mm, where the Q2 percentage was 3.2% lower than the Mesonet percentage (Fig. 3b). This suggests that Q2 overestimated precipitation for light rain events compared to Mesonet observations because the distribution is shifted toward higher precipitation amounts for Q2 estimates. For other bins, the Q2 percentages were slightly higher than the corresponding Mesonet percentages, and the differences became negligible as the precipitation amounts of the bins increased (Fig. 3b).

To evaluate the spatial average of 24-h accumulated precipitation, statewide 24-h total precipitation, the sum of all Mesonet observations (collocated Q2 estimates), are plotted in Fig. 4. This comparison only includes precipitation events (at least one Mesonet station recorded 24-h total precipitation ≥0.25 mm). Similar to the analysis of the individual gauge values in Fig. 1a, a linear relationship between the two datasets was found with a stronger correlation of 0.943 (vs 0.881 in Fig. 2a), which would be expected from a statewide total precipitation comparison with less temporal variability than the individual gauges. Again, Q2 estimates, on average, were higher than Mesonet observations by 34.4% in this comparison. Two outliers appeared in Fig. 4 where the Q2 estimates were 1219 and 3000 mm, while the corresponding statewide Mesonet observations were nearly zero and less than 400 mm, respectively. Further examination into these two outliers using data from the National Climatic Data Center (NCDC) revealed that both outliers occurred during heavy snowfall events over Oklahoma. Because the Mesonet gauges were unheated, they were not able to record the falling frozen

precipitation during these two events. Removal of these outliers from the analysis produces negligible changes in the results.

To further investigate the temporal averages of 24-h accumulated precipitation at each Mesonet station, the average annual precipitation distributions for both Mesonet and Q2 over the entire state of OK during the period 2010–12 are presented in Fig. 5. As illustrated in Fig. 5, Mesonet observations varied from ~300 mm in western Oklahoma to slightly over 1000 mm in eastern Oklahoma (Fig. 5a), whereas Q2 estimates reached around 1500 mm in eastern Oklahoma (Fig. 5b). Mean Q2 precipitation estimates over the state exceeded the mean Mesonet-observed precipitation by 242.4 mm (~35.1%) (Fig. 5c). Q2 estimates were higher than Mesonet observations across most of Oklahoma with a few notable exceptions. In extreme southeastern Oklahoma, the western panhandle, and northwestern Oklahoma to the northeast of the Texas panhandle, Q2 estimates were significantly less than Mesonet observations (Fig. 5c). The Q2 underestimates over these regions are primarily due to poor radar coverage shown in Fig. 6. The regions of significant underestimates are located where the bottom of the base beam height is greater than 1219 m AGL and in some cases exceeds 3000 m AGL (Fig. 6). With the volume scans overshooting much of the falling precipitation in these regions, underestimates occur.

Figure 7 presents the same scatterplot as Fig. 2 except for the samples with good radar coverage. Compared to the results in Fig. 2, the correlations are slightly stronger and the means are slightly higher in Fig. 7. The largest increases in correlation (+0.019) and wet bias (+5.84%) occurred during the cold season, while those during the warm season only increased slightly. It is likely the Q2 estimates during the cold season were impacted more by radar coverage than those during the warm season because precipitating clouds tend to be more shallow (more likely to be overshot by radar) during the cold season.

The impacts of radar coverage on Q2 estimates on an annual time scale are shown by scatterplots of average annual precipitation from collocated Mesonet observations and Q2 estimates at each Mesonet station in Fig. 8. Based on all available radar samples, a linear relationship between Q2 estimates and Mesonet observations was found with a strong correlation of 0.875 (Fig. 8a), although Q2 estimates were still higher than Mesonet observations for most cases. After removing the data points where Mesonet stations were located in the regions of poor radar coverage, the linear relationship still holds and the correlation increases to 0.92 (Fig. 8b). Limiting the comparison to only regions of good radar coverage increases the slope of the regression line in addition to increasing correlation. Note that the difference between Q2 estimates and Mesonet observations in Figs. 4 and 8a are the same (~35%), while the difference

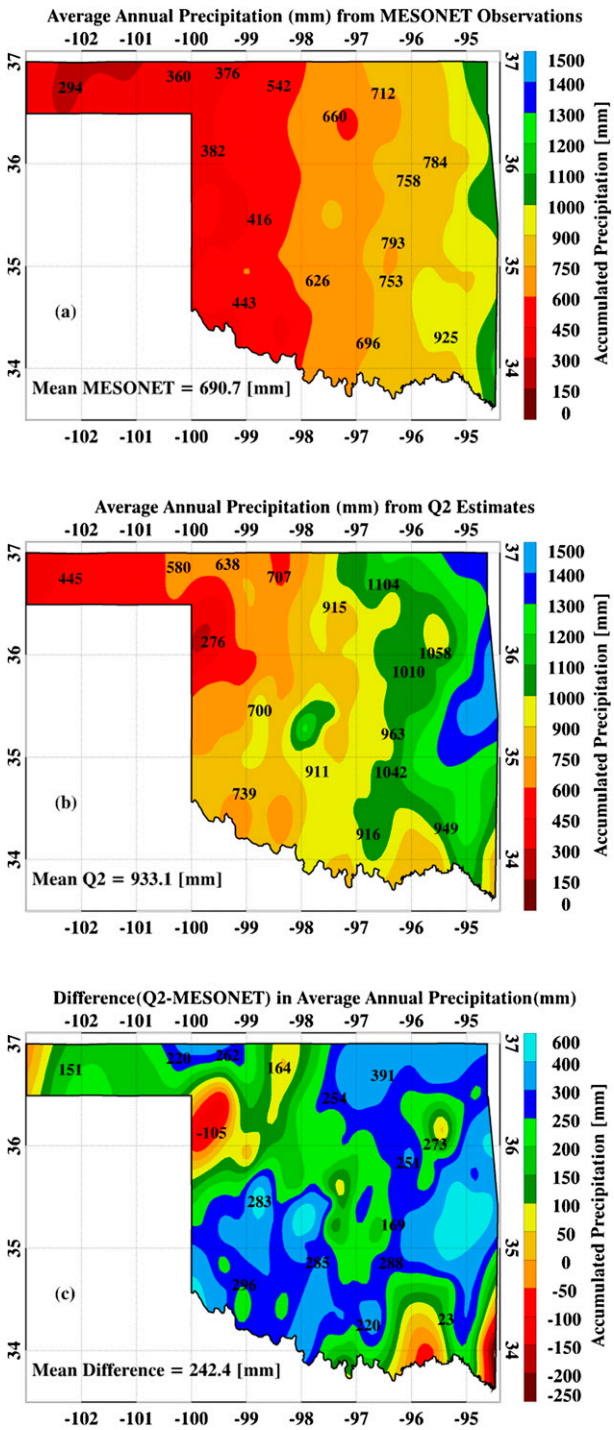

FIG. 5. Average annual precipitation (a) observed by the Oklahoma Mesonet stations, (b) estimated by NEXRAD Q2, and (c) their difference (Q2 − Mesonet) during the period 2010–12.

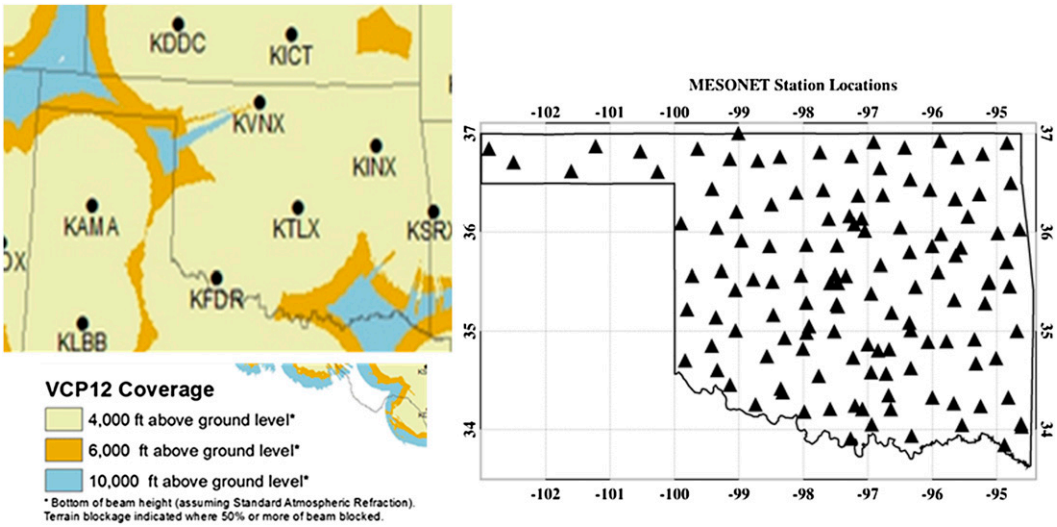

FIG. 6. (left) Image of NEXRAD radar coverage provided by the NOAA NWS Radar Operational Center. Bottom of base beam height assuming standard atmospheric refraction is contoured for volume coverage pattern 12 scans. Light yellow color (good radar coverage in this study) represents coverage with the bottom of base beam height ≤ 4000 ft (1219 m), orange color represents >4000 ft and ≤6000 ft (1829 m), and light blue represents >6000 ft and ≤10 000 ft (3048 m). (right) Location of all Mesonet stations represented by black triangles.

is ~38.6% in Fig. 8b. This result indicates that the actual positive bias of Q2 precipitation estimates may be slightly larger than the value calculated using all qualities of radar coverage.

Examining the Q2-estimated rain distribution yielded results consistent with Mesonet observations. As shown in Table 1, Q2 estimates indicated that ~69.8% of accumulated rainfall occurred in CC regions, compared to ~71.0% observed by Mesonet. The 24.3% of Q2-estimated precipitation fell in SR regions, approximately 0.2% less than what was observed by Mesonet. Q2 estimates indicated ~6.0% of precipitation in non-rain-core regions compared to ~4.4% observed by Mesonet.

b. SCaMPR versus Oklahoma Mesonet

A similar study has been performed to evaluate the SCaMPR retrievals using Mesonet observations for the year 2012. Figure 9 shows CFDs of 24-h accumulated precipitation from SCaMPR and Mesonet with a total of 43 852 collocated samples. The CFD comparison between SCaMPR and Mesonet is similar to that between Q2 and Mesonet in Fig. 3a except that the SCaMPR CFD starts below 80%. Further examination shows that the first bin (0–2 mm) in SCaMPR retrievals is 10% lower than the corresponding Mesonet bin, indicating that SCaMPR retrievals overestimated precipitation for light rain events. For other bins, the SCaMPR percentages are greater than the corresponding Mesonet percentages. These percentage differences are almost an order of magnitude larger than the Q2 versus Mesonet comparison.

A scatterplot for 24-h precipitation retrieved by SCaMPR and observed by Mesonet is presented in Fig. 10a with a modest correlation of 0.489 for a linear relationship. The mean 24-h accumulated precipitation was 25.20 mm for SCaMPR compared to 8.98 mm for Mesonet observations (Fig. 10a). Annual comparisons produced an increase in correlation to 0.567 as shown in Fig. 10b. However, the SCaMPR-retrieved precipitation, on average, is about 3.7 times the Mesonet observations with an annual precipitation of 2431 mm for SCaMPR and 662.6 mm for Mesonet. Nearly 63% of the SCaMPR overestimates across all stations occurred from April to June when precipitation primarily came from intense convection. Statewide 24-h total precipitation comparisons between SCaMPR retrievals and Mesonet observations (Fig. 11) were consistent with their annual precipitation comparison at each Mesonet station. The mean statewide 24-h total precipitation was 1090.29 mm for SCaMPR and 304.19 mm for Mesonet, roughly the same ratio as their annual precipitation, but with a stronger correlation of 0.665.

The precipitation distribution from SCaMPR estimates was significantly different from the Mesonet-observed precipitation distribution, as shown in Table 1. A large dry bias occurred in the CC region, where only ~12.2% of SCaMPR-estimated precipitation fell compared to the ~71.0% observed by Mesonet. However, a significant wet bias occurred in the non-rain-core

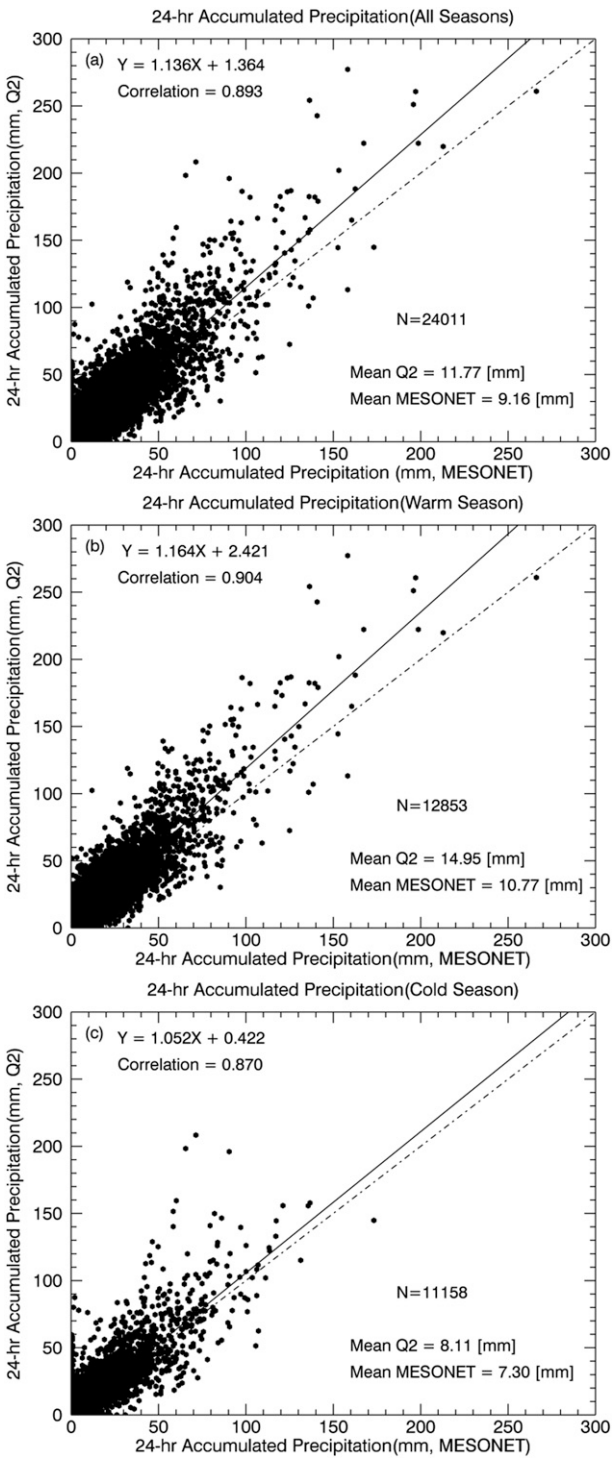

FIG. 7. As in Fig. 1, but for the data collected over regions with good radar coverage demonstrated in Fig. 6.

regions where SCaMPR-estimated precipitation was 57.1% versus the ~4.4% observed by Mesonet. For the SR region, the SCaMPR-estimated precipitation percentage was 30.7%, only 6.1% greater than the Mesonet-observed percentage. Inclusion of relative humidity (RH) corrections into the SCaMPR algorithm reduced the amount of precipitation in non-rain-core regions by ~13.0%.

4. Discussion

Despite having a wet bias, Q2 estimates were very strongly correlated with Mesonet observations, while SCaMPR estimates suffered from a very large wet bias likely owing to excessive precipitation retrievals from anvil regions of DCSs. Q2 estimates were strongly correlated with Mesonet observations for 24-h accumulated precipitation at each Mesonet station (0.881), statewide 24-h total precipitation (0.943), and average annual precipitation (0.92). Q2 estimates were consistently higher (~35%) than collocated Mesonet observations regardless of time scale (24 h vs annual) and spatial coverage (one Mesonet station vs all Oklahoma Mesonet stations), particularly during the warm season when more intense convection occurred. However, despite these consistent overestimates, the distribution of precipitation into the DCS regions from Q2 estimates closely matched Mesonet observations, particularly in the convective-core and stratiform regions. Slight differences occurred in the anvil cloud region, where the tipping-bucket limitations (0.25 mm) in Mesonet observations would create bias-favoring rain-core precipitation over non-rain-core precipitation. This bias likely occurs because AC precipitation is typically light and may not accumulate >0.25 mm within 5 min to trigger the tipping bucket, while Q2 estimates do not face this limitation. As a result, the Mesonet-observed AC precipitation is slightly lower than reality, while the Mesonet-observed CC and SR precipitation are slightly higher than reality. SCaMPR retrievals were weakly correlated to Mesonet observations at the 24-h time scale and modestly correlated at an annual time scale. Regardless of time scale, SCaMPR retrievals drastically overestimated precipitation compared to Mesonet observations. Furthermore, the distribution of SCaMPR retrievals showed a strong dry bias for rain-core regions and a strong wet bias for anvil regions.

Although insignificant in this study, sampling errors are possible when comparing both the 1 km × 1 km grid resolution of Q2 estimates and the 4 km × 4 km grid resolution of SCaMPR retrievals to point observations from Mesonet. For example, intense precipitation could occur over part of the grid box where the Mesonet station is not located, making the gridbox estimate higher than the point observation. On the other hand, the most intense precipitation could occur over the Mesonet station, making the gridbox estimate less than the point

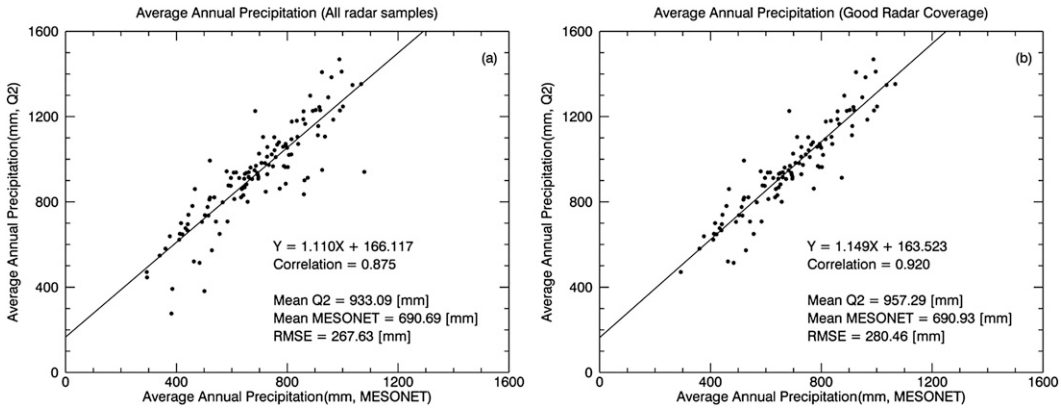

FIG. 8. Each dot represents the average annual precipitation (2010–12) observed at a Mesonet station and the collocated Q2 estimate for a grid box of 1 km × 1 km containing the Mesonet station. (a) All available collocated Mesonet and Q2 observations ($N1 = 119$) and (b) only for the stations ($N2 = 106$) after removing data points where Mesonet stations were located in the regions of poor radar coverage (bottom of base beam height >1219 m AGL).

observation. While errors such as these are unavoidable for this study and similar studies, with a sufficiently large sample size these errors of representativeness will tend to balance one another over a long time period. As the location of the precipitation maxima inside the grid box can be viewed as random, the expected value of total precipitation at the station and the total precipitation in the grid box will be equal. Part of this impact is likely apparent in the trend of observing stronger correlations between the estimates and observations as the time scale of comparison was increased. While this source of error does not appear to be very significant for this study, it could require special attention for studies utilizing much smaller sample sizes for comparison.

a. Strengths and weaknesses of Q2 estimates

The strong correlations between Q2 estimates and Mesonet observations regardless of time scale or spatial coverage make it possible to use Q2 estimates as a substitute for surface rain gauge networks in the studies where finer spatial and temporal resolution is needed. However, the 35% wet bias in Q2 estimates must be considered, although it is likely an upper bound of the Q2 estimate errors because rain gauges are prone to underestimate rainfall during intense precipitation events (www.mesonet.org/index.php/site/about/moisture_measurements). Furthermore, with simple linear relationships between Q2 estimates and Mesonet observations, Q2 estimates could be easily adjusted to better represent ground truth. However, further studies are required to quantitatively determine the magnitude of Q2 overestimates and the catchment errors associated with tipping-bucket rain gauges used in the OK Mesonet during different seasons (Humphrey et al. 1997; Nešpor and Sevruk 1999; Sevruk 1985; Steiner et al. 1999). Based on this study, bias-adjusted Q2 estimates in the regions such as the southern Great Plains and U. S. Southeast should be reliable because precipitation is mainly in liquid phase and dominated by convective events, where the highest correlations between Q2 estimates and Mesonet observations were found.

The primary weakness of Q2 estimates is a discontinuity in precipitation estimates depending on available radar coverage. While Q2 estimates have strong correlations with Mesonet observations in the regions of good radar coverage, this is not true in the areas where radar coverage is less sufficient. As the base beam height of the available radar coverage increased, Q2 estimates shift from overestimates to underestimates compared to Mesonet observations. This change reduces the correlations from 0.92 for good radar coverage to 0.875 for all radar samples, as illustrated in Fig. 6. Although the correlation for all radar samples is still strong, caution must be taken because underestimates in regions of poor radar coverage may mask the tendency of Q2 to overestimate. As the base beam height increases, the

TABLE 1. Distribution of observed and estimated rainfall among DCS components. Constructed using data from 16 days with widespread convection over Oklahoma during 2012. SCaMPR RH represents SCaMPR with corrections using modeled RH. The percentage represents the amount of total rainfall that fell in each DCS region.

	Rainfall per region (%)			
Platform	CC	SR	AC	Unclassified/thin anvil
Mesonet	71.01	24.55	2.46	1.97
Q2	69.75	24.31	4.46	1.49
SCaMPR	12.23	30.68	35.21	21.88
SCaMPR RH	15.46	40.48	31.15	12.91

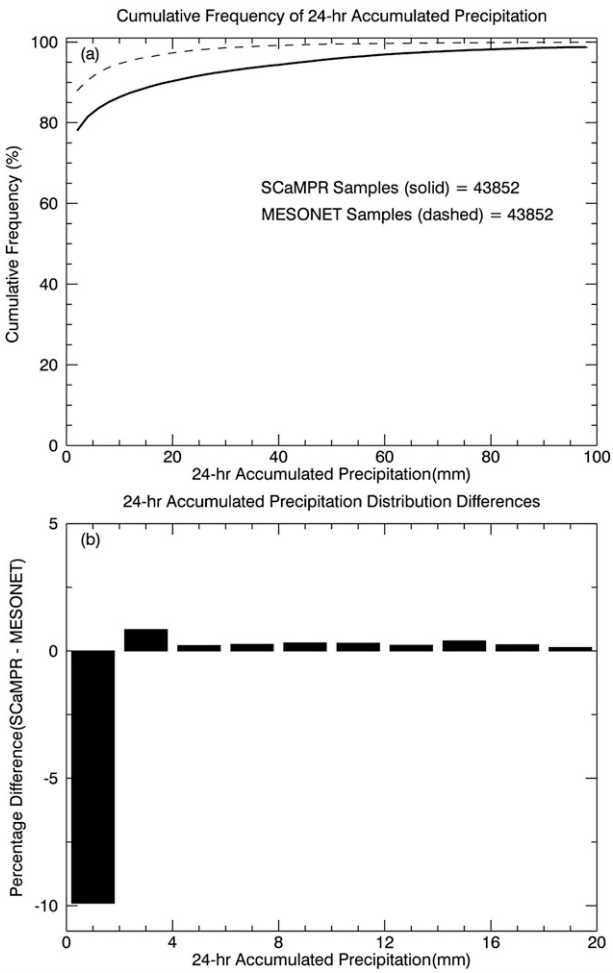

FIG. 9. As in Fig. 2, but for the collocated SCaMPR retrievals and Mesonet observations for 2012.

probability that precipitation will be overshot and therefore underestimated by Q2 also increases. While the magnitude of this difference is not significantly large in most cases, depending on the specific use of Q2 estimates, this factor should be carefully considered when using estimates from the regions of poor radar coverage.

b. *Evaluation of SCaMPR*

SCaMPR retrievals overestimated precipitation at all Mesonet stations for 2012, with overestimates of annual precipitation ranging from 1400 to 2000 mm (Fig. 10b). Correlations between SCaMPR retrievals and Mesonet observations were relatively low on an annual time scale (0.567) and even lower at a 24-h time scale (Fig. 10a). While the direct comparison between the SCaMPR 4 km × 4 km pixels and point observations from Mesonet stations may reduce the correlations to some degree, the low correlations arise primarily from SCaMPR precipitation retrievals during the following situations. Quite often SCaMPR-retrieved precipitation from the anvil regions of DCSs, while the collocated Mesonet stations recorded nothing. This is apparent in Table 1, where the majority of SCaMPR-estimated precipitation occurred in non-rain-core regions. These excessive precipitation retrievals from anvil regions are most likely due to the limitation of SCaMPR retrievals arising from SCaMPR's dependence on cloud-top IR brightness temperature, which is similar for both rain-core and anvil regions of the DCSs. This problem, as well as possible cirrus contamination, could be responsible for the majority of SCaMPR overestimates during DCS events (Zhang et al. 2013). Therefore, it is necessary to quantitatively estimate the SCaMPR retrievals (and Q2 estimates) under different precipitation ranges using collocated Mesonet observations as ground truth. In an unpublished study, we found that there is a much lower incidence of false alarms than in this study when comparing the full version of the algorithm using SEVIRI data with TRMM data (B. Kuligowski 2013, unpublished study). This suggests that the SCaMPR algorithm will likely perform better when it is run on the GOES-R Advanced Baseline Imager instead of on the current GOES imager.

c. *Categorical scores for Q2 and SCaMPR*

Categorical scores were calculated for both the 24-h accumulated Q2 precipitation estimates and SCaMPR retrievals using thresholds of 0.25, 2.5, 12.5, and 25.0 mm from Mesonet observations. Probability of detection (POD), false alarm rate (FAR), and critical success index (CSI) were calculated for each of these thresholds. The Q2 categorical scores were computed for two periods, 2010–12 and 2012 only, while SCaMPR retrieval categorical scores were calculated only for 2012 to allow a direct comparison to the Q2 estimates. As shown in Table 2, progressing from the 2.5-mm threshold to the 25.0-mm threshold, both POD and CSI of Q2 estimates decreased while FAR increased. This observed trend is consistent with the Wu et al. (2012) results, but the decreased magnitudes in POD are significantly different. In the Wu et al. study PODs dropped significantly as the threshold level increased, while the POD decreased only 0.04 from 0.85 to 0.81 in this study. Using 0.25 mm as an additional threshold that was not used in the Wu et al. (2012) study, a relatively high FAR of 0.37 for Q2 estimates was observed. This relatively large FAR is most likely attributed to very light precipitation that evaporated before reaching the ground and occasional ground clutter problems [as demonstrated in Fig. 12 caused by beam ducting from temperature inversions (Turton et al. 1988)]. Figure 12 represents an example when clear skies were present over Oklahoma, but Q2 indicated precipitation.

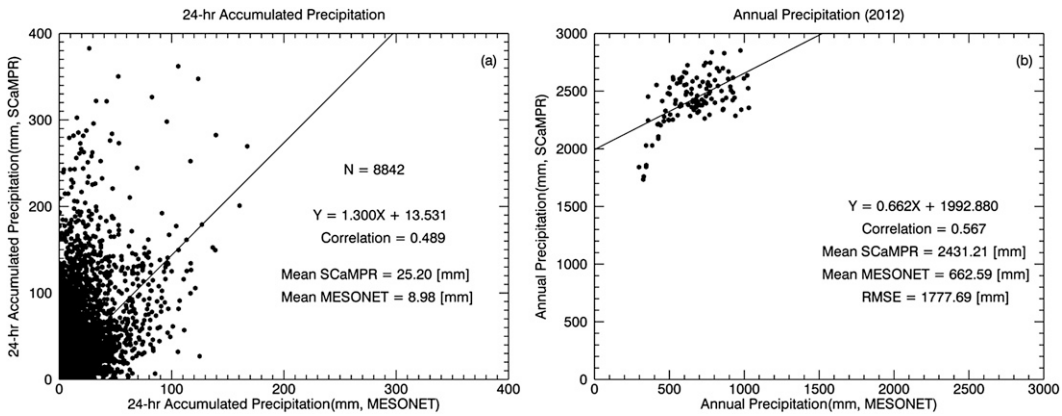

FIG. 10. (a) As in Fig. 2a, but for SCaMPR retrievals and Mesonet observations for 2012. (b) As in Fig. 8a, but for SCaMPR retrievals and Mesonet observations for 2012.

Although the contribution of Q2 overestimates from ground clutter is quite small (Fig. 12), a binary precipitation/no precipitation threshold was used to identify this issue in the FAR and CSI scores.

The categorical scores for SCaMPR retrievals were consistent with expectations based on the large overestimates from precipitation retrievals in nonprecipitating regions of DCSs. FARs increased as the threshold level increased, ranging from 0.50 at the 0.25-mm threshold to 0.83 at the 25.0-mm threshold. This increase can be attributed to retrievals of heavy precipitation from nonprecipitating and lightly precipitating portions of DCSs, which cause the FAR to increase as the frequency of heavy precipitation retrievals drop more slowly than actual occurrences of these events. Although SCaMPR POD scores were high and close to Q2 values, FAR scores rose to 0.83 at the 25.0-mm threshold, resulting in much lower CSI scores (0.16). Therefore, it is important to improve the SCaMPR retrieval algorithms in the future, particularly for the conditions that produce high FAR and low CSI scores.

An analysis of RMSEs for both Q2 and SCaMPR was consistent with expectations based on the skill scores and linear regression fits. As shown in Table 3, both Q2 and SCaMPR RMSEs rose as the amount of recorded precipitation increased. For the 0.25–2.5 mm precipitation bin in Table 3, the SCaMPR RMSE (10.26 mm) is nearly 8 times the Q2 RMSE (1.30 mm). This large difference in RMSE between Q2 and SCaMPR can be attributed to SCaMPR precipitation retrievals in nonprecipitating regions of DCSs. As illustrated in Fig. 13f, SCaMPR-retrieved precipitation is very similar to the GOES, cloud-top, IR temperatures (Fig. 13c) and overestimates the precipitation over the AC regions, such as northern Missouri and eastern Arkansas owing to cold cloud-top temperatures, whereas Q2 estimates (Fig. 13d) and a modified SCaMPR algorithm (Fig. 13e) showed nothing over this region.

The modified SCaMPR algorithm, employing both cloud optical depth and IR brightness temperature, can significantly reduce the spatial extent of the SCaMPR-estimated precipitation, particularly over the anvil regions of DCSs. As illustrated in Figs. 13e and 13f, the SCaMPR precipitation areas were reduced to 31% in the modified version from 48% in its original algorithm (IR temperature only). The new coverage is very close to the Q2-estimated precipitation coverage (33%, Fig. 13d). A more robust comparison covering 14 convective events over Oklahoma during the Midlatitude Continental Convective Clouds Experiment (MC3E) campaign has also shown the improvements of the modified SCaMPR (Fig. 14). As demonstrated in Fig. 14, the probability density functions (PDFs) of the rain area

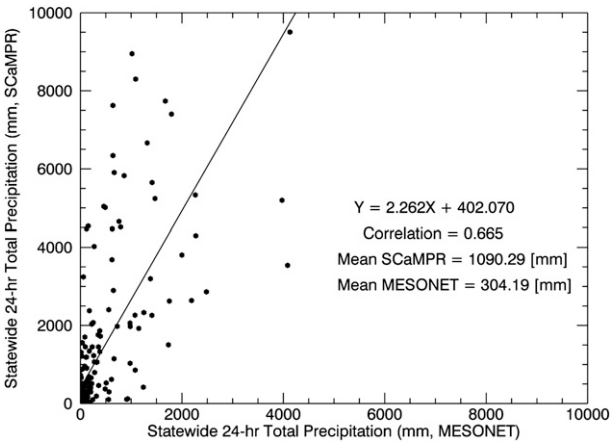

FIG. 11. As in Fig. 4, but for SCaMPR retrievals and Mesonet observations for 2012 (N = 261).

TABLE 2. Categorical scores for SCaMPR-retrieved precipitation (2012), Q2 estimates (2010–12), and Q2 estimates (2012) for 24-h periods.

Range (mm)	Q2 POD (all)	Q2 FAR (all)	Q2 CSI (all)	SCaMPR POD (2012)	Q2 POD (2012)	SCaMPR FAR (2012)	Q2 FAR (2012)	SCaMPR CSI (2012)	Q2 CSI (2012)
≥0.25	0.78	0.37	0.53	0.75	0.83	0.50	0.37	0.43	0.56
≥2.5	0.85	0.27	0.64	0.81	0.89	0.59	0.24	0.37	0.69
≥12.5	0.84	0.31	0.61	0.83	0.84	0.72	0.31	0.26	0.61
≥25.0	0.81	0.40	0.53	0.78	0.80	0.83	0.42	0.16	0.51

from the modified version are very close to those from Q2 estimates, while those from the original SCaMPR algorithm are significantly lower at the 10% bin and significantly higher in the 40% bin. For example, nearly 60% of the events were estimated to have rain area percentages less than 10% by Q2 and the new algorithm, while only ~40% of events were estimated to have rain area percentages less than 10% by SCaMPR retrievals. On average, the precipitation area estimated from the modified algorithm (9.64%) is closer to the Q2 estimation (12.06%) than that (19.11%) from the SCaMPR original algorithm. This new algorithm and further analysis of its performance will be discussed in much greater detail in future work.

On the annual and average annual time scales, RMSE values were consistent with the overestimates seen from both statewide and station to gridbox comparisons. For Q2, the RMSE for average annual comparisons was 267.6 mm, and the average was 280.5 mm when using comparisons only in regions of good radar coverage as shown in Fig. 7. RMSE was actually higher in regions of good radar coverage because the tendency of Q2 overestimating precipitation was not diminished by the overshooting of precipitation in the regions of poor radar coverage. Although RMSE was slightly higher, correlation was stronger between Q2 and Mesonet in regions of good radar coverage. The RMSE for Q2 statewide comparisons was 308.8 mm. Again, the SCaMPR RMSE was significantly higher (1777.7 mm), as expected for the annual station to grid box comparison as shown in Fig. 9.

5. Conclusions and future work

With the immensely better spatial and temporal coverage and resolution compared to rain gauge networks, and the strong correlations with gauge observations, Q2 estimates can serve as a reasonable substitute for ground truth to validate satellite precipitation retrievals in the future as long as the 35% wet bias in Q2 estimates is adequately adjusted or accounted for. Although Q2 estimates were higher than Mesonet observations during the warm season, an excellent agreement was reached for the cold season, and there were strong correlations in both seasons. Additionally, the precipitation distribution among deep convective system components from Q2-estimated precipitation strongly resembled the Mesonet-observed distribution. The similarity of the precipitation distributions indicates that, although Q2 has a wet bias in this region, it can accurately capture the precipitation characteristics of DCSs. As Q2 estimates accurately depict the precipitation distribution among the components of DCSs, they can be used to evaluate improvements in precipitation distribution

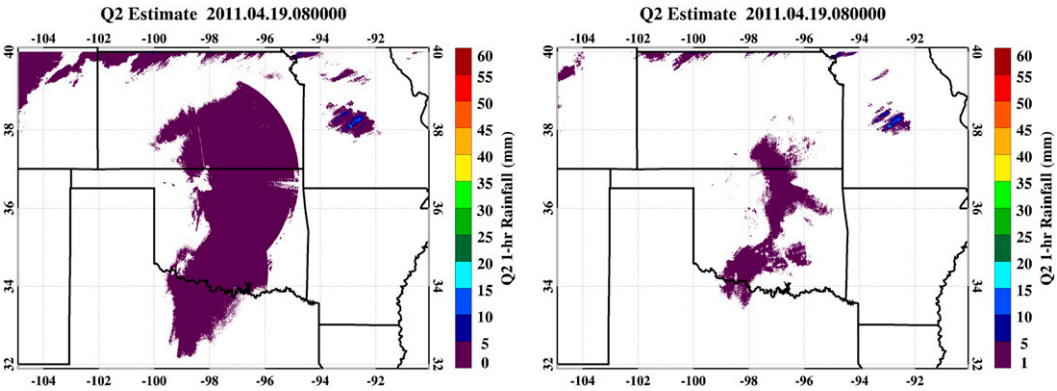

FIG. 12. An illustration of the ground clutter contribution to Q2-estimated precipitation with precipitation starting at (left) 0 and (right) 1 mm. At this time clear skies were reported over Oklahoma.

TABLE 3. RMSE for 24-h Q2 and SCaMPR estimates. The ranges used for the calculations are determined from the Mesonet observations. Q2 RMSE is shown for all data (2010–12) and for only 2012 data.

Range (mm)	Q2 RMSE (all) (mm)	Q2 RMSE (2012) (mm)	SCaMPR RMSE (2012) (mm)
$0 \leq x < 2.5$	1.07	1.30	10.26
$2.5 \leq x < 12.5$	7.09	7.20	36.59
$12.5 \leq x < 25$	11.73	12.82	55.44
$25 \leq x$	21.62	24.27	61.03

characteristics made in future modifications to SCaMPR. Furthermore, with the Mesonet stations likely underestimating the true precipitation amounts during DCSs, the wet bias calculated for Q2 during this study is likely an upper bound. While these overestimates could be adjusted using the best-fit linear regression equations, further studies are needed to determine the extent of required adjustments. The catchment errors in Mesonet observations should be carefully analyzed and considered before adjusting Q2 estimates (Sevruk 1985; Nešpor and Sevruk 1999; Humphrey et al. 1997).

Minor ground clutter issues were detected, but the contribution of ground clutter to Q2 precipitation estimates was negligible. It also seemed that virga could possibly be causing Q2 overestimates during light precipitation events or in cases where no precipitation was observed. Again, this effect was very minor, producing only very small overestimates at times. However, caution should be taken in using Q2 estimates for binary rain/no rain distinction at a threshold value of 0.25 mm if conditions are conducive to producing ground clutter such as temperature inversions (Turton et al. 1988).

SCaMPR retrievals were much higher than the collocated Mesonet observations, by a factor of 3–5 times. The severe overestimates in SCaMPR retrievals were primarily caused by precipitation retrievals over the anvil regions of DCSs when collocated Mesonet stations recorded no precipitation. This problem is most apparent in the precipitation distributions among DCS components where the majority of SCaMPR-estimated precipitation falls in anvil regions rather than the rain-core regions. These precipitation retrieval problems contributed significantly to the high FAR and lower CSI for SCaMPR retrievals. The bulk of these overestimates mainly occurred from April to June, which had frequent intense convective systems. As POD scores are already quite high, reducing the FAR would make SCaMPR a valuable and reliable source of precipitation estimates.

The problem of excessive SCaMPR-estimated precipitation rates over the anvil regions of DCSs can be corrected by utilizing NMQ Q2 estimates and GOES cloud optical depth and IR temperature retrievals. A strong optical depth gradient was found between the precipitating and nonprecipitating (anvil) regions of DCSs, although their cloud-top temperatures are

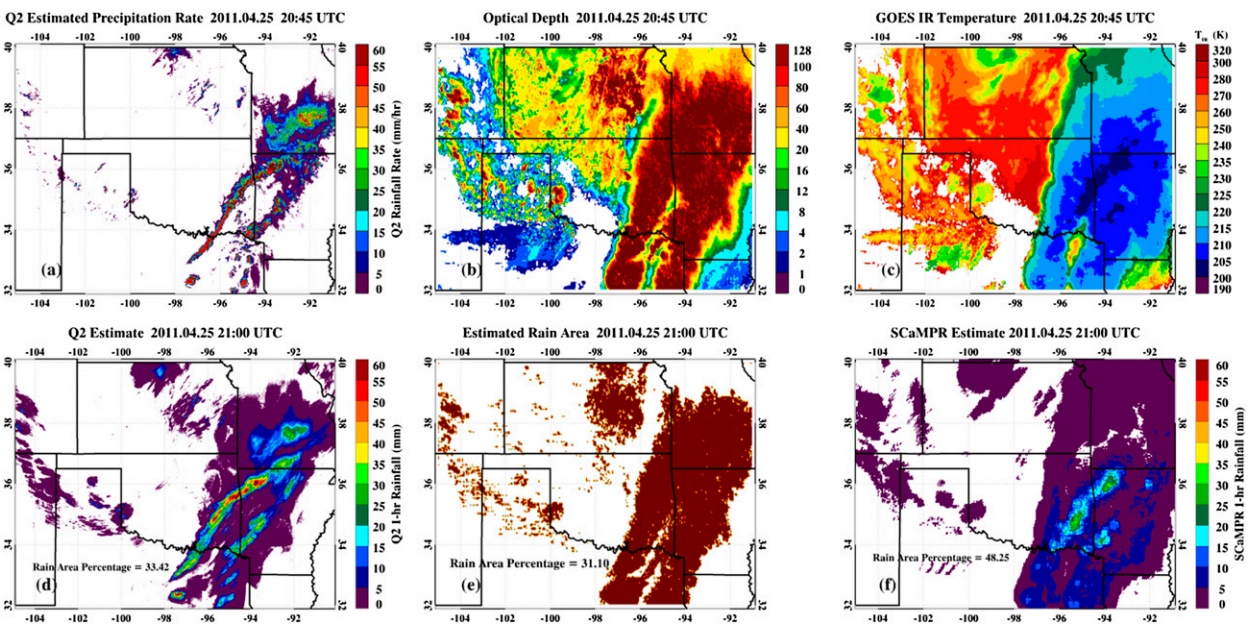

FIG. 13. Instantaneous (a) Q2-estimated precipitation rate (mm h^{-1}), (b) GOES-retrieved cloud optical depth, and (c) IR temperature (K) at 2045 UTC 25 Apr 2011. Accumulated (d) Q2-estimated rainfall (areal coverage 33.4%), (e) estimated rain area (31.1%) from the newly developed algorithm using both cloud optical depth and IR brightness temperature, and (f) SCaMPR-retrieved rainfall (areal coverage 48.3%) over the large domain during 2000–2100 UTC 25 Apr 2011.

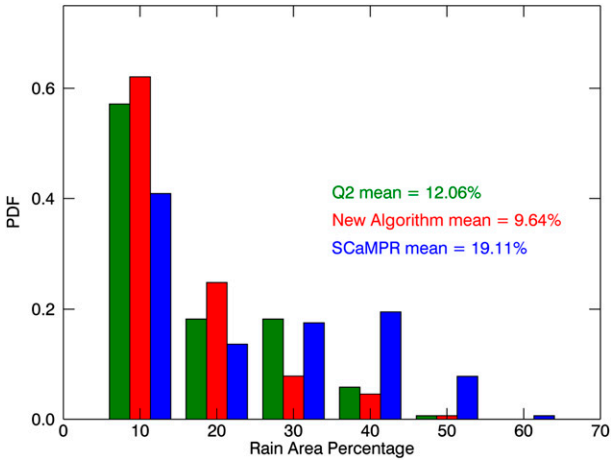

FIG. 14. PDFs of rain area over the SGP using a bin width of 10% during the MC3E campaign (14 days with convection). The 0.25-mm threshold was used for both Q2 and SCaMPR to determine whether or not a pixel was classified as raining.

nearly the same. This strong gradient can be used to identify the precipitating and nonprecipitating regions of a DCS. Preliminary testing of this method has shown significant reductions in the precipitating area that will reduce the percentage of non-rain-core precipitation (Fig. 14). While cloud optical depth does appear to better capture the spatial features of precipitating areas, IR brightness temperature is still superior in providing information about the intensity of precipitation (Fig. 13c).

Similar studies for other regions of the CONUS should be performed to investigate the similarities and differences in precipitation characteristics of DCSs between the SGP and other regions. These studies will provide insights into potential regional similarities and differences in DCSs that can be used for algorithm development and forecasting. With the NWS radar network now having dual-polarization capabilities, hail cores could also be added as a DCS component, possibly allowing further understanding of DCSs. Additionally, the new algorithm developed and additional modifications to SCaMPR will be evaluated in future work using the hybrid classifications and Q2 estimates as a source of validation data.

Acknowledgments. Oklahoma Mesonet precipitation observations were obtained from the Atmospheric Radiation Measurement Program sponsored by the U.S. Department of Energy Office of Energy Research, Office of Health and Environmental Research, Environmental Sciences Division. The NEXRAD Q2 product was obtained from the NOAA National Severe Storms Laboratory. This research was primarily supported by NOAA GOES-R project with Award Number NA11NES440004 at the University of North Dakota. The University of North Dakota authors were also supported by DOE ASR project with Award Number DE-SC0008468. The contents of this paper are solely the opinions of the authors and do not constitute a statement of policy, decision, or position on behalf of NOAA or the U.S. government.

REFERENCES

Adler, F. R., and A. J. Negri, 1988: A satellite infrared technique to estimate tropical convective and stratiform rainfall. *J. Appl. Meteor.,* **27,** 30–51, doi:10.1175/1520-0450(1988)027<0030:ASITTE>2.0.CO;2.

Amitai, E., W. Petersen, X. Llort, and S. Vasiloff, 2012: Multiplatform comparisons of rain intensity for extreme precipitation events. *IEEE Trans. Geosci. Remote Sens.,* **50,** 675–686, doi:10.1109/TGRS.2011.2162737.

Andrieu, H., J. D. Creutin, G. Delrieu, and D. Faure, 1997: Use of a weather radar for the hydrology of a mountainous area. Part I: Radar measurements interpretation. *J. Hydrol.,* **193,** 1–25, doi:10.1016/S0022-1694(96)03202-7.

Austin, P. M., 1987: Relation between measured radar reflectivity and surface rainfall. *Mon. Wea. Rev.,* **115,** 1053–1070, doi:10.1175/1520-0493(1987)115<1053:RBMRRA>2.0.CO;2.

Chen, S., and Coauthors, 2013: Evaluation and uncertainty estimation of NOAA/NSSL Next-Generation National Mosaic Quantitative Precipitation Estimation Product (Q2) over the continental United States. *J. Hydrometeor.,* **14,** 1308–1322, doi:10.1175/JHM-D-12-0150.1.

Feng, Z., X. Dong, B. Xi, C. Schumacher, P. Minnis, and M. Khaiyer, 2011: Top-of-atmosphere radiation budget of convective core/stratiform rain and anvil clouds from deep convective systems. *J. Geophys. Res.,* **116,** D23202, doi:10.1029/2011JD016451.

——, ——, ——, S. McFarlane, A. Kennedy, B. Lin, and P. Minnis, 2012: Life cycle of deep convective systems in a Lagrangian framework. *J. Geophys. Res.,* **117,** D23201, doi:10.1029/2012JD018362.

Hong, Y., R. F. Adler, A. Negri, and G. J. Huffman, 2007: Flood and landslide applications of near real-time satellite rainfall products. *Nat. Hazards,* **43,** 285–294, doi:10.1007/s11069-006-9106-x.

Huffman, G. J., and Coauthors, 2007: The TRMM Multisatellite Precipitation Analysis (TMPA): Quasi-global, multiyear, combined-sensor precipitation estimates at fine scales. *J. Hydrometeor.,* **8,** 38–55, doi:10.1175/JHM560.1.

Humphrey, M. D., J. D. Istok, J. Y. Lee, J. A. Hevesi, and A. L. Flint, 1997: A new method for automated dynamic calibration of tipping-bucket rain gauges. *J. Atmos. Oceanic Technol.,* **14,** 1513–1519, doi:10.1175/1520-0426(1997)014<1513:ANMFAD>2.0.CO;2.

Islam, T., and M. A. Rico-Ramirez, 2013: An overview of the remote sensing of precipitation with polarimetric radar. *Prog. Phys. Geogr.,* **38,** 55–78, doi:10.1177/0309133313514993.

Joyce, R. J., J. E. Janowiak, P. A. Arkin, and P. Xie, 2004: CMORPH: A method that produces global precipitation estimates from passive microwave and infrared data at high spatial and temporal resolution. *J. Hydrometeor.,* **5,** 487–503, doi:10.1175/1525-7541(2004)005<0487:CAMTPG>2.0.CO;2.

Kirstetter, P.-E., and Coauthors, 2012: Toward a framework for systematic error modeling of spaceborne precipitation radar with NOAA/NSSL ground radar–based National Mosaic QPE. *J. Hydrometeor.,* **13,** 1285–1300, doi:10.1175/JHM-D-11-0139.1.

Kondragunta, C. R., D. Kitzmiller, D. J. Seo, and K. Shrestha, 2005: Objective integration of satellite, rain gauge, and radar precipitation estimates in the multisensor precipitation estimator algorithm. Preprints, *19th Conf. on Hydrology,* San Diego, CA, Amer. Meteor. Soc., P2.8. [Available online at https://ams.confex.com/ams/Annual2005/techprogram/paper_86219.htm.]

Krajewski, W., and J. Smith, 2002: Radar hydrology: Rainfall estimation. *Adv. Water Resour.,* **25,** 1387–1394, doi:10.1016/S0309-1708(02)00062-3.

Kubota, T., and Coauthors, 2007: Global precipitation map using satelliteborne microwave radiometers by the GSMaP project: Production and validation. *IEEE Trans. Geosci. Remote Sens.,* **45,** 2259–2275, doi:10.1109/TGRS.2007.895337.

Kuligowski, R. J., 2010: GOES-R Advanced Baseline Imager (ABI) algorithm theoretical basis document for rainfall rate (QPE). NOAA/NESDIS/STAR Rep., 44 pp. [Available online at www.goes-r.gov/products/ATBDs/baseline/Hydro_RRQPE_v2.0_no_color.pdf.]

Langston, C., J. Zhang, and K. Howard, 2007: Four-dimensional dynamic radar mosaic. *J. Atmos. Oceanic Technol.,* **24,** 776–790, doi:10.1175/JTECH2001.1.

Maddox, R., J. Zhang, J. Gourley, and K. Howard, 2002: Weather radar coverage over the contiguous United States. *Wea. Forecasting,* **17,** 927–934, doi:10.1175/1520-0434(2002)017<0927:WRCOTC>2.0.CO;2.

Negri, A. J., and R. F. Adler, 1981: Relationship of satellite-based thunderstorm intensity to radar-estimated rainfall. *J. Appl. Meteor.,* **20,** 288–300, doi:10.1175/1520-0450(1981)020<0288:ROSBTI>2.0.CO;2.

Nešpor, V., and B. Sevruk, 1999: Estimation of wind-induced error of rainfall gauge measurements using a numerical simulation. *J. Atmos. Oceanic Technol.,* **16,** 450–464, doi:10.1175/1520-0426(1999)016<0450:EOWIEO>2.0.CO;2.

Park, H. S., A. V. Ryzhkov, D. S. Zrnić, and K.-E. Kim, 2009: The hydrometeor classification algorithm for the polarimetric WSR-88D: Description and application to an MCS. *Wea. Forecasting,* **24,** 730–748, doi:10.1175/2008WAF2222205.1.

Scofield, R. A., and R. J. Kuligowski, 2003: Status and outlook of operational satellite precipitation algorithms for extreme-precipitation events. *Wea. Forecasting,* **18,** 1037–1051, doi:10.1175/1520-0434(2003)018<1037:SAOOOS>2.0.CO;2.

Sevruk, B., 1985: Correction of precipitation measurements. *Proc. Workshop on the Correction of Precipitation Measurements,* Zurich, Switzerland, WMO/IAHS/ETH, 13–23.

Smith, J. A., D. J. Seo, M. L. Baeck, and M. D. Hudlow, 1996: An intercomparison study of NEXRAD precipitation estimates. *Water Resour. Res.,* **32,** 2035–2045, doi:10.1029/96WR00270.

Sorooshian, S., K. Hsu, X. Gao, H. V. Gupta, B. Imam, and D. Braithwaite, 2000: Evaluation of PERSIANN system satellite-based estimates of tropical rainfall. *Bull. Amer. Meteor. Soc.,* **81,** 2035–2046, doi:10.1175/1520-0477(2000)081<2035:EOPSSE>2.3.CO;2.

Steiner, M., R. A. Houze, and S. E. Yuter, 1995: Climatological characterization of three-dimensional storm structure from operational radar and rain gauge data. *J. Appl. Meteor.,* **34,** 1978–2007, doi:10.1175/1520-0450(1995)034<1978:CCOTDS>2.0.CO;2.

——, J. A. Smith, S. J. Burges, C. V. Alonso, and R. W. Darden, 1999: Effect of bias adjustment and rain gauge data quality control on radar rainfall estimation. *Water Resour. Res.,* **35,** 2487–2503, doi:10.1029/1999WR900142.

Turk, F. J., E. E. Ebert, H.-J. Oh, B.-J. Sohn, V. Levizzani, E. A. Smith, and R. Ferraro, 2003: Validation of an operational global precipitation analysis at short time scales. Preprints, *12th Conf. on Satellite Meteorology and Oceanography,* Long Beach, CA, Amer. Meteor. Soc., JP1.2. [Available online at https://ams.confex.com/ams/annual2003/techprogram/paper_56865.htm.]

Turton, J. D., D. A. Bennetts, and S. F. G. Farmer, 1988: An introduction to radio ducting. *Meteor. Mag.,* **117,** 245–254.

Vicente, G. A., R. A. Scofield, and W. P. Menzel, 1998: The operational GOES infrared rainfall estimation technique. *Bull. Amer. Meteor. Soc.,* **79,** 1883–1898, doi:10.1175/1520-0477(1998)079<1883:TOGIRE>2.0.CO;2.

Villarini, G., and W. Krajewski, 2010: Review of the different sources of uncertainty in single polarization radar-based estimates of rainfall. *Surv. Geophys.,* **31,** 107–129, doi:10.1007/s10712-009-9079-x.

Wu, D., X. Dong, B. Xi, Z. Feng, A. Kennedy, G. Mullendore, M. Gilmore, and W.-K. Tao, 2013: Impacts of microphysical scheme on convective and stratiform characteristics in two high precipitation squall line events. *J. Geophys. Res. Atmos.,* **118,** 11 119–11 135, doi:10.1002/jgrd.50798.

Wu, W., D. Kitzmiller, and S. Wu, 2012: Evaluation of radar precipitation estimates from the National Mosaic and Multisensor Quantitative Precipitation Estimation System and the WSR-88D precipitation processing system over the conterminous United States. *J. Hydrometeor.,* **13,** 1080–1093, doi:10.1175/JHM-D-11-064.1.

Zhang, J., and Y. Qi, 2010: A real-time algorithm for the correction of brightband effects in radar-derived QPE. *J. Hydrometeor.,* **11,** 1157–1171, doi:10.1175/2010JHM1201.1.

——, K. Howard, and J. J. Gourley, 2005: Constructing three-dimensional multiple-radar reflectivity mosaics: Examples of convective storms and stratiform rain echoes. *J. Atmos. Oceanic Technol.,* **22,** 30–42, doi:10.1175/JTECH-1689.1.

——, and Coauthors, 2011: National Mosaic and Multi-Sensor QPE System: Description, results, and future plans. *Bull. Amer. Meteor. Soc.,* **92,** 1321–1338, doi:10.1175/2011BAMS-D-11-00047.1.

——, and Coauthors, 2014: Initial operating capabilities of quantitative precipitation estimation in the multi-radar multi-sensor system. *28th Conf. of Hydrology,* Atlanta, GA, Amer. Meteor. Soc., JP5.3. [Available online at https://ams.confex.com/ams/94Annual/webprogram/Paper240487.html.]

Zhang, Y., D.-J. Seo, D. Kitzmiller, H. Lee, R. J. Kuligowski, D. Kim, and C. R. Kondragunta, 2013: Comparative strengths of SCaMPR satellite QPEs with and without TRMM ingest versus gridded gauge-only analyses. *J. Hydrometeor.,* **14,** 153–170, doi:10.1175/JHM-D-12-053.1.

Zrnić, D. S., V. M. Melnikov, and A. V. Ryzhkov, 2006: Correlation coefficients between horizontally and vertically polarized returns from ground clutter. *J. Atmos. Oceanic Technol.,* **23,** 381–394, doi:10.1175/JTECH1856.1.